International Journal of Heat and Mass Transfer 228 (2024) 125644

Contents lists available at ScienceDirect

International Journal of Heat and Mass Transfer

journal homepage: www.elsevier.com/locate/ijhmt

Heat, mass and momentum transport in wet mineral-wool insulation: Experiment and simulation

Fan Lu [a], Massoud Kaviany [a,*], John Williams [b], Thomas Addison-Smith [b]

[a] Department of Mechanical Engineering, University of Michigan, Ann Arbor, MI 48109, United States
[b] Aspen Aerogels, East Providence, RI 02914, United States

ARTICLE INFO

Keywords:
Heat transfer in wet insulation
Water submerged insulation behavior
Drying
Drying front regime
Liquid saturation
Capillary pressure

ABSTRACT

To test the performance of wet mineral-wool insulation, a water submersion setup is used to monitor its heat transfer sequentially through dry, submerged, and drainage-drying periods. A cylindrical-shell insulation is wrapped around a pipe carrying a preheated (over 100 °C) oil stream. The temperature at various locations is monitored, and after a few hours in each period, steady-state conditions are reached.

Numerical 2-D (with gravity) simulations of the transient, simultaneous heat, mass, and momentum transport are also performed, with the control of the insulation hydrophobicity through the insulation surface liquid saturation. The distributions of temperature, liquid saturation, liquid and vapor velocity, vapor mass fraction, and evaporation rate, are predicted as well as the total heat flow through the dry/wet insulation. The predicted heat flow rate and temperature distribution within the insulation, through the three periods, are in good agreement in heat flow rate and temperature distributions with the test results (maximum difference of 20 %).

The predicted 2-D liquid saturation shows that gravity and capillary pressure play significant roles in the liquid distribution and the insulation hydrophobicity changes with temperature due to the dissolution of the hydrophobic fiber coating. The presence of a gap between the pipe and insulation plays a significant role in heat transfer during the submerged period, as it allows for continuous direct liquid contact with the pipe. During the drying period, the evaporation rate continuously decreases (with a decrease in the average liquid saturation), governed by the increasing resistances to the heat and liquid flow.

1. Introduction

Heat loss from outdoor, hot fluid transporting pipes subject to humidity and precipitation accounts for major industrial energy loss. It is recognized that under slightest mobile liquid water content this heat loss from the open-cell thermal insulation increases substantially; and search continues for solutions to control this effect and heat loss in superheated steam transport network, reducing the related industrial energy consumption. We estimate that the US refineries, chemical plants, power stations, and other industrial facilities employ nearly 40 million sqm of hot-service pipe insulation. Comprised primarily of mineral wool, fiberglass, and calcium silicate, these materials insulate outdoor equipment and piping systems operating between ambient and 650°C. If healthy, that inventory would leak 7.4 GW of thermal energy. However, based on more than 15 years of our field surveys, the proposing team has evidence that total heat losses are nearly double that value. Due to the near-ubiquitous presence of moisture within these systems, the actual losses from hot industrial insulation is about 0.2% of total domestic energy consumption. While the plant-wide energy audits are done, they tend to focus on fixed and rotating equipment (boilers, columns, pumps, etc.) rather than the interconnecting piping systems, losing more heat than the design value, ranging as high as +250%. In every case the culprit was moisture in the insulation, even in systems operating above 500°C.

Thus, accidental and undesirable wetting of thermal insulation wrappings occur in outdoor (field) applications under moist conditions, and this increases the thermal conductivity [1] and deteriorates the insulation performance. Water penetrates the insulation with no outside lining, or through the lining seams, or seams between segmented insulation. The distribution of the water within the insulation greatly affects the thermal performance of the wet insulation.

Water (wetting fluid) penetrates the insulation due to gravity (including buoyancy) and capillary pressure and this movement (motion) is opposed by the viscous drag using the permeability (the Darcy law). The permeability, including the relative permeabilities for two-

* Corresponding author.
E-mail address: kaviany@umich.edu (M. Kaviany).

https://doi.org/10.1016/j.ijheatmasstransfer.2024.125644
Received 8 July 2023; Received in revised form 16 April 2024; Accepted 26 April 2024

Nomenclature

A	area (m^2)
c_p	specific heat (J/kg-K)
D	diameter (m)
D_m	mass diffusion coefficient (m^2/s)
f	inverse relaxation time (s^{-1})
g	gravitational acceleration, 9.81 m/s^2
h	heat transfer coefficient (W/m^2-K) enthalpy (J/kg)
H	depth of the center of the hot pipe (m)
Δh_{lg}	heat of evaporation (J/kg)
K	absolute permeability (m^2)
K_r	relative permeability
k	thermal conductivity (W/m-K)
L, l	length (m)
M	mass (kg)
$\dot{M}$	mass flow rate (kg/s)
$\dot{m}$	mass flux vector (kg/m^2-s)
$\dot{n}$	volumetric evaporation rate (kg/m^3-s)
p	pressure (Pa)
Q	heat flow rate (W)
Q_i	oil heat loss rate (W)
q	heat flux (W/m^2)
R	radius (m)
R_g	gas constant (J/kg-K)
R_{ku}	surface convection resistance (K/W)
R_{Du}	mass transfer resistance (K-s/kg)
Le	Lewis number
S_l	normalized saturation
s	saturation
r	radius (m)
T	temperature (°C)
t	time (s)
u	velocity (m/s)
V	volume (m^3)
w	width (m)
x_i	fraction of species i
y	vertical position (m)

Greek symbols

α	phase volume fraction, Thermal diffusivity
ε	porosity
μ	viscosity (Pa-s)
ρ	density (m^3/kg)
σ	surface tension (N/m)
θ	angular position
θc	contact angle (°)

Subscripts

a	ambient
c	capillary, condenser
d	dry
dn	downstream
ext	external
f	fluid
g	gas/vapor, guard
gud	guard
ng	noncondensible gas
i	inner boundary
ir	irreducible
k	conduction
l	liquid
lg	saturation
m	mass
max	maximum
o	outer boundary, oil
p	pore, pipe
s	surface, solid
t	thermal
u	convection
up	upstream Others
$\langle . \rangle$	spatial average

phase flows, accounts for the local volume fraction of the phases. The pore volume fraction of water (wetting-phase) is called the liquid saturation, s_l, and varies from zero for dry insulation to one for completely liquid filled insulation. The relative permeabilities and the capillary pressure are functions of s_l. For insulations wrapped around heated surfaces, this undesirable water evaporates. Thus, the thermal performance of the wet insulation is governed by the transient, simultaneous two-phase heat, mass, and momentum transport, a challenging analysis.

The deterioration of the thermal performance of wet insulation results in much energy loss and cost in insulation for industrial and habitant applications, causing a continuous search for new materials [2]. A classification of the thermal insulation material into inorganic (foamy and fibrous), organic (foamy and foamy-expanded), combined (e.g., siliconized calcium), and new technology materials (e.g., transparent, dynamic) is given in [3]. Aerogels (e.g., silica) offer low thermal conductivity and significant heat loss saving [4] and are fire retardant. Moistures in insulation cause significant damage to metallic pipes they insulate (the corrosion under insulation) [5], especially in the oil and gas industry where these transport lines are exposed to the natural elements including rain [6].

Recent tests conducted by Aspen Aerogel reveal that submerged wet insulation experiences over 30-fold greater heat loss compared to the dry insulation. Further analyses and simulations are required to elucidate the underlying cause of this substantial heat loss.

To quantify the insulation performance deterioration caused by the moisture, water submersion and drying tests were performed in [7], and the effective thermal conductivity, and temperature and liquid saturation distributions in a horizontal, cylindrical-shell mineral wool was measured. They found the effective thermal conductivity of the wet mineral wool is 50-fold larger than the dry sample. They also found higher liquid saturation in the lower half of the wet insulation, due to gravity.

Regarding previous numerical simulations of the thermal behavior of moisture transfer through porous insulation, A transient modeling of the coupled heat and moisture transfer was performed in [8], while others have predicted a increase in the effective thermal conductivity with the moisture content [9,10], However, the substantial heat loss observed in submerged wet insulation experiments has not been predicted by models.

While the fundamentals of two-phase flow, phase change, and heat transfer through porous media are relatively well known [11], application to transient, three-dimensional geometries and estimate of the effective properties such as the capillary pressure, remain challenging [11]. Pore network model of imbibition and drying of porous media has been used, mostly in transient 2-D simulations, involving a limited number of pores [12]. The volume-averaged treatments (using representative an elementary volume, over which the local porosity and gas and saturations are defined) allow for inclusion of larger volumes, but remain computationally very demanding.

Here to characterize (measurement and analysis) the thermal

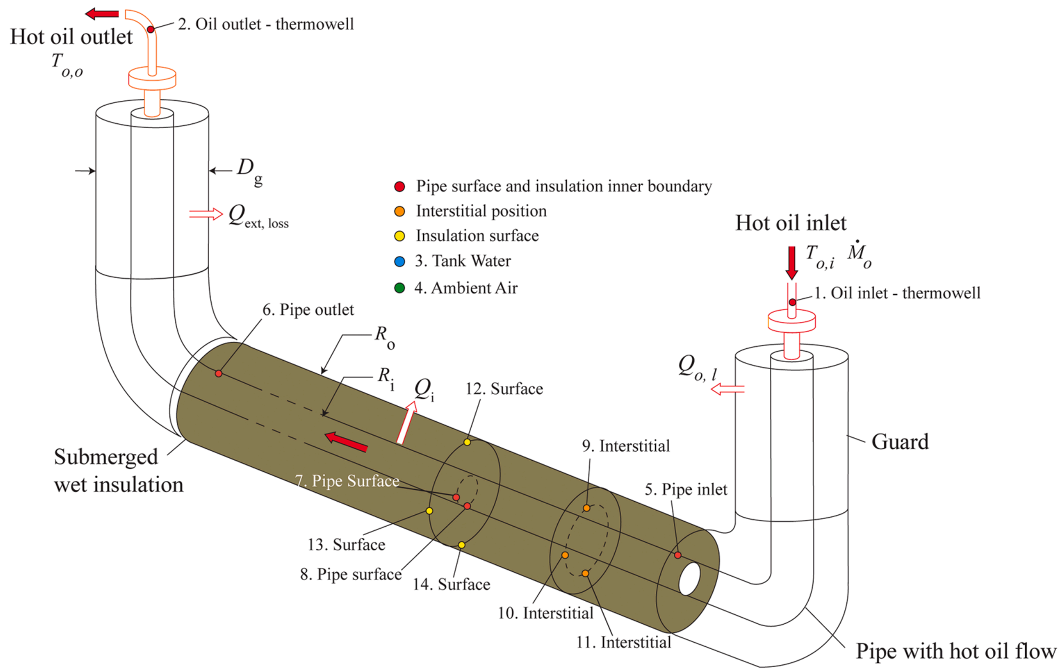

Fig. 1. A schematic rendering of the test section. Hot oil flows through a stainless tube and first encounters a stainless steel cased (guard) insulated region which is partially submerged in water. Then insulation-wrapped test section is followed by a rising guard-insulation section. The locations of the thermocouples (and their number designation) are also shown. The heat flowing into the wrapped insulation section is designated as Q_i.

behavior of wet mineral wool insulation, a wetting-heating setup is built allowing for complete soaking and complete drying of insulation samples. The tests are performed in three sequential periods, namely, heating of dry, water submerged, and drained-drying insulation. The heat flow rate and temperature distributions during these three periods are measured. CFD analyses of the related transient simultaneous transport phenomena are also performed in both 2-D and 3-D domains, and compared with the test results. The incorporation of the phase change, capillary pressure models (e.g., van Genuchten), momentum, thermal non-equilibrium between phases, and gravity, into the simulations beyond simple 1-D domains, are among the new treatments presented here.

2. Experiment and tests

2.1. Heated pipe, insulation, and water bath

To characterize the thermal performance of the wet mineral wool insulation, a cylindrical shell insulation is wrapped around a heated pipe. The test is schematically shown in Fig. 1. The portion of the heated pipe shown includes the test section as well as well-insulated upstream and downstream sections (stainless-steel guards containing multilayer of perlites insulation). The oil is heated by Joule (electrical resistance) heating elements and pumped into the pipe, entering at temperature $T_{o,i}$ and exiting at temperature $T_{o,o}$, locations 1 and 2 in Fig. 1. This is implemented using a Mokon 350 series Thermal Fluid System (including temperature control), and a JV-KG positive displacement, spur-gear flowmeter (recording the oil flow rate). This oil stream heat loss is

$$Q_{o,u} = \dot{M}_o c_{p,\ o}\left(T_{o,i} - T_{o,o}\right), \tag{1}$$

where $\dot{M}_o$ is the oil mass flow rate.

Some of this heat is lost upstream and downstream of the insulation wrapping, and this oil stream heat loss, $Q_{o,l}$, is estimated from the measured temperature of the related surface. Both surface natural (thermobuoyant) convection and radiation heat transfer are included in the estimate and discussed in Appendix B.

The temperature recorded at different axial and angular locations in the wet insulation are numbered 5 to 14 in Fig. 1. Thermocouples 5-8 (red) measure the pipe surface temperature at various axial locations, while 9-11 (orange) are the interstitial (between insulation layers) locations, $(R_o + R_i)/2$. Thermocouples 12- 14 (yellow) are on the insulation surface, while 3 (blue) measures the water temperature in the tank, and 4 (green) measures the ambient temperature. The ambient temperature affects $Q_{o,l}$. The pipe surface temperature is also designated with T_i. The symbols are defined in the Nomenclature.

During the submerged period, due to thermal buoyancy, the water at the top of the tank can have a higher temperature (thermal stratification). To avoid this, a mixer is used to keep the tank water temperature uniform.

Table 1 lists the insulation geometric parameters and properties, the heated pipe fluid, the submersion tank, and test conditions, with the related variables defined.

Table 1
Wet-insulation test conditions, geometry, temperatures, materials, and equipment.

Geometry	Insulation inner and outer radii, R_i , R_o (cm)	4.45, 9.53
	Insulation length, L (cm)	124
	Guard diameter, D_g (cm)	16.5
	Gap size (mm)	0.44
Temperatures	Oil inlet temperature, $T_{o,i}$ (°C)	167
	Ambient temperature, T_a (°C)	25
Hot oil stream (DELF 600)	Mass flow rate, $\dot{M}_o$ (kg/s)	0.089
	Specific heat, $c_{p,\ o}$(J/kg-K) [13]	2370
Mineral wool (Rockwool ProRox PS 960)	Permeability, K (m^2) [14–16]	2.5×10^{-10}
	Effective thermal conductivity, $\langle k \rangle_d$ (W/m-K) [17]	0.035
	Porosity, ε	0.95
	Specific heat, c_p (J/kg-K) [17]	128
Thermocouples	Omega TC Probe type K	
Water Tank	TARTER 170 Gallen water tank	
Thermal-Fluid system	Mokon 350 Series	
Flowmeter	JV-KG positive displacement spur-gear meter	

2.2. Sequential dry, submerged, and drainage-drying periods

The test is a sequential scenario of dry, water submerged, and drainage-drying periods. The insulation has no outside lining and there exists a gap between the pipe and the insulation, where water can reach and contact the pipe through the seams. This gap is not necessarily symmetric, but is assumed as such for modeling purposes. This is rendered in Fig. 2. The gap between the pipe and insulation occurs in all applications. The estimate of the average gap size can be for example from [18]. This standard accounts for the maximal tolerance stack of pipe outside and insulation inside diameter by mandating a minimal gap between the two. The minimum gap for our 3-inch pipe is 0.44 mm [18]. During the dry (liquid saturation $s_l = 0$) period, heat transfers through the insulation Q_i by conduction, with the effective thermal conductivity $\langle k \rangle$ of the mineral wool being both density $\langle \rho \rangle$ and temperature dependent [19], while the specific heat $\langle c_p \rangle$ is constant. In the submerged period, liquid penetrates the insulation by gravity (hydrostatic pressure and buoyancy) and capillary pressure, and after a short time, the maximum liquid saturation is reached. While there is evaporation adjacent to the heated surface (the pipe carries a hot oil stream with temperature over 100°C), there is a liquid saturation gradient that persists to the steady state. The vapor vents through the outer boundary of the insulation. In the drainage-drying period, the liquid initially leaves the lower outer boundary by gravity while resisted by capillary pressure. The capillary pressure model is adjusted to match the dripping drainage observed in the experiment. The liquid drainage loss rate decreases exponentially. At the end of the drainage subperiod, i.e., during the drying subperiod, the remaining water has a higher liquid saturation in the lower portion of the insulation, and the water loss is by evaporation only. The vapor transport across the outer boundary is governed by the simultaneous heat and mass transfer (related to the ambient relative humidity and temperature, and the outer surface cools down). After a few hours, the irreducible liquid saturation is reached, and the drying is governed by advancing drying fronts, moving from the heated surface toward the outer surface. Irreducible saturation refers to the minimum liquid saturation that remains trapped within the pore spaces of a porous media, which is also called immobile saturation [11]. The dry front is a radial location separating the region of no liquid, i.e., dry region ($s_l = 0$), from the wet region ($s_l > 0$), and moves toward the outer radius with increasing elapsed time, during the latter part of the drying period.

3. Heat, mass, and momentum transport in partially saturated porous media

The transient heat transfer through the wet insulation is by conduction, convection (advection), and phase change (evaporation and condensation). Compared with the volume averaging method widely used in porous media simulations [21] for separate gas-mixture and liquid phase velocities, we use the numerical computer software Fluent (from ANSYS, Release 17.2) [22] with the two-phase flow treated with the Eulerian method. Within the Eulerian treatment, multiple phases coexist within a domain, and each phase is treated as a separate continuum with its own set of governing equations [22]. The Finite Volume Method (FVM) is applied to discretize the spatial domain of for the conservation of momentum, heat, and mass. For the volume fraction formulation, the Implicit Formulation is chosen to achieve a better stability. Considering the rather low velocity field inside the insulation, the Laminar Model is selected as the viscous treatment.

The local phase volume fraction of the liquid and gas phases are α_l

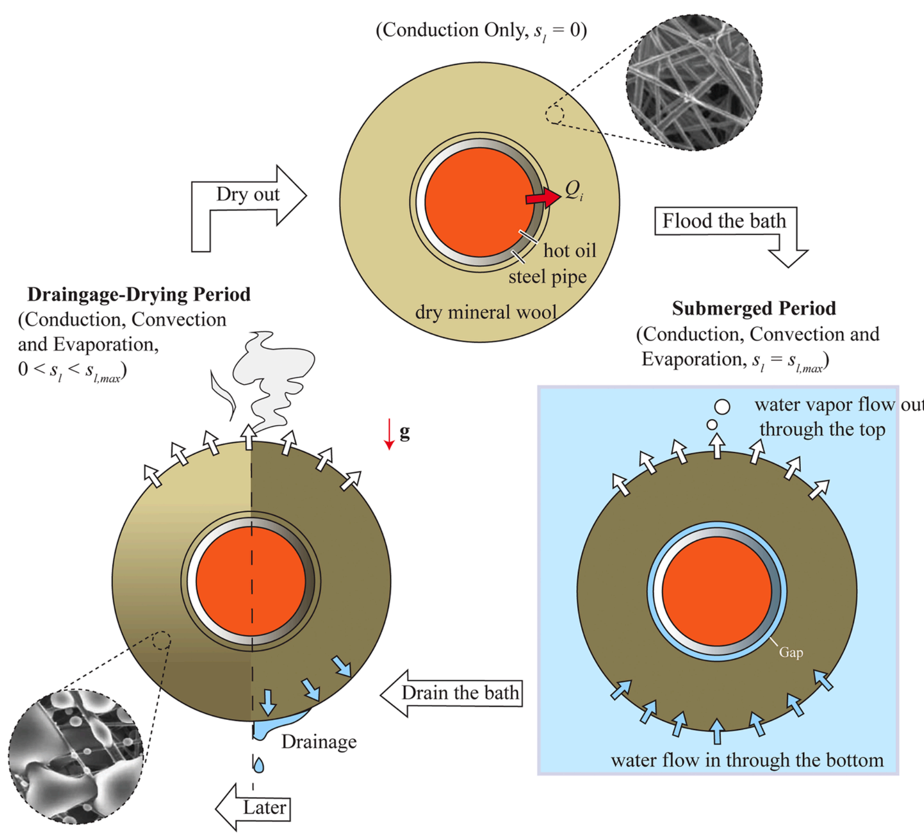

Fig. 2. Rendering of the wet mineral wool insulation wraps around a heated pipe. The thermal characterization is divided into three sequential dry, submerged, and drainage-drying periods. The wetted fibrous insulation is also shown, indicating the hydrophobicity of the fibers which influences the contact angle, relative permeabilities, and capillary pressure. In the dry period, the liquid saturation is zero, while in the submerged period, it reaches its maximum value and during drainage-dry period the liquid saturation decreases till complete drying which corresponds to liquid saturation of zero [20].

and α_g, and vary between zero and $1-\varepsilon$, where ε is the porosity. Since there are three phases, solid, liquid, and vapor, then

$$\alpha_l+\alpha_g+\alpha_s=1 \quad (2)$$

$$\alpha_l+\alpha_g=1-\varepsilon, \quad (3)$$

while s_l and s_g are the local volume fractions of the liquid and gas phase in the pore volume, such that

$$s_l \;+\; s_g \;=\; 1. \quad (4)$$

Then,

$$s_l=\frac{\alpha_l}{1-\varepsilon},\; s_g=\;\frac{\alpha_g}{1-\varepsilon}, \quad (5)$$

The simultaneous heat, mass, and momentum conservation equations, and the related constitutive equations (such as the relative permeability and capillary pressure) are listed in the following section.

3.1. Governing equations, properties, and CFD

3.1.1. Fluent governing equations

The conservation equation for species (mass), momentum, and energy, applied under the velocity slip between the gas and liquid phases, and local thermal equilibrium among the solid, gas, and liquid phases are listed below.

The continuity equation (mass conservation) [22] for liquid is

$$\frac{\partial\varepsilon\alpha_l\rho_l}{\partial t}+\nabla\cdot(\varepsilon\alpha_l\rho_l\boldsymbol{u}_l)=-\varepsilon\dot{n}_{lg}\Rightarrow\frac{\partial\alpha_l\rho_l}{\partial t}+\nabla\cdot(\alpha_l\rho_l\boldsymbol{u}_l)\;=-\dot{n}_{lg}, \quad (6)$$

where ε is the porosity and $\dot{n}_{lg}$ is the volumetric phase change (evaporation) rate.

The gas mixture continuity equation is

$$\frac{\partial(\alpha_g\rho_g)}{\partial t}+\nabla\cdot(\alpha_g\rho_g\boldsymbol{u}_g)=\dot{n}_{lg}\,. \quad (7)$$

The momentum conservation in each phase is [22] ($i = l, g$)

$$\frac{\partial}{\partial t}(\varepsilon\alpha_i\rho_i\boldsymbol{u}_i)+\nabla\cdot(\varepsilon\alpha_i\rho_i\boldsymbol{u}_i\boldsymbol{u}_i)=-\varepsilon\alpha_i\nabla(p-p_c)+\varepsilon\alpha_i\rho_i g-\varepsilon^2\alpha_q^2\frac{\mu_i\boldsymbol{u}_i}{KK_{r,i}}, \quad (8)$$

where $\boldsymbol{g}$ is the gravity vector, p_c and μ_i are the capillary pressure and viscosity, and K is the absolute permeability and $K_{r,i}$ is the relative permeability of phase i [23]:

$$K_{r,l}=S_l^q, \quad (9)$$

where q is the Corey exponent, and S_l is the normalized (effective) liquid saturation and $s_{l,ir}$ is the irreducible liquid saturation [23], i.e.,

$$S_l=\frac{s_l-s_{l,ir}}{1-s_{l,ir}}. \quad (10)$$

A similar relation is written for the gas-phase relative permeability.

In the gas mixture phase, there are two species, air (non-condensible) and water vapor (condensible). The gas-phase species conservation equation is [24]

$$\frac{\partial}{\partial t}(\varepsilon\alpha_g\rho_g x_{H_2O})+\nabla\cdot(\varepsilon\alpha_g\rho_g\boldsymbol{u}_g x_{H_2O})=-\nabla\cdot(\varepsilon\alpha_g\dot{\boldsymbol{m}}_{g,H_2O}\;)+\varepsilon\dot{n}_{lg}, \quad (11)$$

Where $\dot{\boldsymbol{m}}_{g,H_2O}$ is the vapor mass flux vector, and x_{H_2O} is the volume fraction of the water vapor.

3.2. Simplified governing equations

Continuity equation, if assume constant liquid density,

$$\rho_l\varepsilon\frac{\partial s_l}{\partial t}+\rho_l\nabla\cdot\boldsymbol{u}_l=-\dot{n}_{lg} \quad (12)$$

$$\varepsilon\frac{\partial\rho_g(1-s_l)}{\partial t}+\nabla\cdot\rho_g\boldsymbol{u}_g=\dot{n}_{lg}\;. \quad (13)$$

The momentum conservation equation is simplified into ($i = l, g$)

$$\boldsymbol{u}_i=-\frac{K_iK_{i,r}}{\mu_i}(\nabla p_i+\rho_i\boldsymbol{g}). \quad (14)$$

The energy equation is

$$\left[(\varepsilon)\frac{(\rho c_p)_s}{(\rho c_p)_l}+\varepsilon s_l+\varepsilon(1-s_l)\right]\frac{\partial T}{\partial t}+\left\{\boldsymbol{u}_l+\left[\frac{(\rho c_p)_{cg}+(\rho c_p)_{ng}}{(\rho c_p)_l}\boldsymbol{u}_g\right]\right\}\cdot\nabla T+\frac{\Delta h_{lg}\dot{n}_{lg}}{(\rho c_p)_l}=\langle\alpha\rangle\nabla^2T. \quad (15)$$

where $\langle\alpha\rangle$ is the total effective thermal diffusivity and $\langle\alpha\rangle = \langle\frac{\langle k\rangle\langle s_l\rangle}{\rho c_p}\rangle$, here the thermal conductivity $\langle k\rangle$ varies linearly with liquid saturation [22], the dry value is listed in Table 1.

The species conservation for the non-condensable gas component is

$$\varepsilon\frac{\partial\rho_{ng}(1-s_l)}{\partial t}+\nabla\cdot(\rho_{ng}\boldsymbol{u}_g)=\nabla D_m\rho_g\cdot\nabla\left(\frac{\rho_{ng}}{\rho_g}\right), \quad (16)$$

where D_m is the mass diffusion coefficient, and ρ_{ng} is the density of noncondensible gas, which is basically air.

3.2.1. Capillary Pressure Model

The capillary pressure relation used is van Genuchten model [25]

$$p_c=p_{c,o}\left[(S_l)^{-\frac{1}{m}}-1\right]^{\frac{1}{n}}, \quad (17)$$

where $p_{c,o}$ is the entry pressure, n is related to the pore size distribution, $m\;=1-1/n$, and S_l is defined in Eq. (10).

3.2.2. Evaporation mechanism: Lee model

Vapor mass conservation

$$\varepsilon\frac{\partial\rho_g(1-s)}{\partial t}+\nabla\cdot\rho_g\boldsymbol{u}_g=\dot{n}_{lg}$$

Based on the Lee model [26]

$$\dot{n}_{lg}=\begin{cases} f\alpha_l\rho_l\dfrac{T-T_{lg}}{T_{lg}}, & T\;>T_{lg} \\ -f\alpha_g\rho_g\dfrac{T_{lg}-T}{T_{lg}}, & T\;<T_{lg}, \end{cases} \quad (18)$$

where f is the frequency. The Lee model [26] is commonly used for evaporation (boiling) and condensation and is implemented in Fluent. It predicts evaporation and condensation rate and is robust with low computation demand. The phase-change mass flux, Eq. (18), contains a tunable frequency f, with default values recommended in Fluent.

When the local temperature (gas-mixture) is above the saturation temperature, the evaporation rate is positive, and the liquid changes to vapor. Conversely, when the local temperature is below the saturation temperature, the evaporation rate (condensation occurs).

T_{lg}, which is the saturation temperature, can be found with Clausius Clapeyron relation

$$\ln\left(\frac{p_0}{p_g}\right)\;=-\frac{\Delta h_{lg}}{R_g}\left(\frac{1}{T_0}-\frac{1}{T_{lg}}\right), \quad (19)$$

where p_0 and T_0 are the reference vapor pressure and temperature, and R_g is gas constant.

3.2.3. Mass transfer boundary condition

The outer surface of the insulation is the only exit of water vapor and

Table 2
The three CFD simulation models, namely, Model 1 assumes axisymmetric transport (no gravity effect), Model 2 with gravity, and Model 3 includes gravity and the tank in the simulation. The figures show the liquid saturation during the submerged period under (large elapsed time) the steady state, using Models 1, 2, and 3.

	Model 1: 1-D (axisymmetric), no gravity	Model 2: 2-D with gravity and no tank	Model 3: 2-D with gravity and tank
Predicted liquid saturation distribution	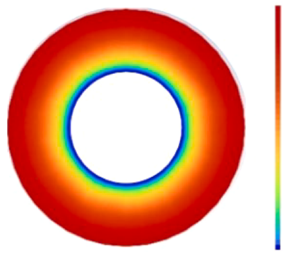	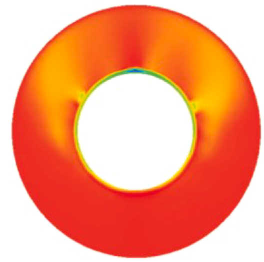	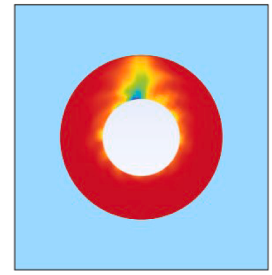
Boundary saturation during submerged period	• Relevant for dry period • Does allow for prescribed surface saturation • Does not allow for observed angular variation of temperature	• Does allow for prescribed surface saturation • Does allow for observed angular variation of temperature	• Does not allow for prescribed surface saturation • Does allow for observed angular variation of temperature • Does include the water tank

heat. It is a surface convection controlled by the heat and mass transfer coefficients, which are coupled by the Lewis number. The condensable gas species mass flow rate at the outer surface is [19]

$$\dot{M}_{cg} = \frac{(\rho_{cg}/\rho_g)_s - (\rho_{cg}/\rho_g)_a}{\langle R_{Du}\rangle_L}, \tag{20}$$

where $(\rho_{cg}/\rho_g)_s$and $(\rho_{cg}/\rho_g)_a$ are the mass fraction of water vapor (condensing gas species) at the outer surface of and in the ambiance, respectively, and ρ_{cg} is the mass density of water vapor. Here $\langle R_{Du}\rangle$ is the mass transfer resistance between the surface and the ambient.

The heat and species resistances are coupled [19]

$$\langle R_{Du}\rangle_L = \langle R_{ku}\rangle_L c_{p,f}\mathrm{Le}^{-\frac{2}{3}},\ \ \mathrm{Le} = \frac{D_{m,A}}{\alpha_f}\ . \tag{21}$$

where Le is the Lewis number, α_f is the thermal diffusivity, and $D_{m,A}$ is the mass diffusivity.

The surface-convection resistance is [20]

$$\langle R_{ku}\rangle_L = \frac{1}{hA}, \tag{22}$$

where h is the heat transfer coefficient, and is determined based on the outer surface air flow condition (thermobuoyant or forced flow).

Table 3
Comparison of measured and predicted temperature at various locations at the end of the dry period (steady state).

Location	Experiment, T (°C)	Prediction, T (°C)	Location	Experiment, T (°C)	Prediction, T (°C)
1	161.9	–	8	169	167
2	158.8	–	9	87.0	87.3
3	–	–	10	85.9	87.3
4	15.3	–	11	92.2	87.3
5	166	167	12	28.2	28.0
6	167	167	13	29.1	28.0
7	168	167	14	27.5	28.0

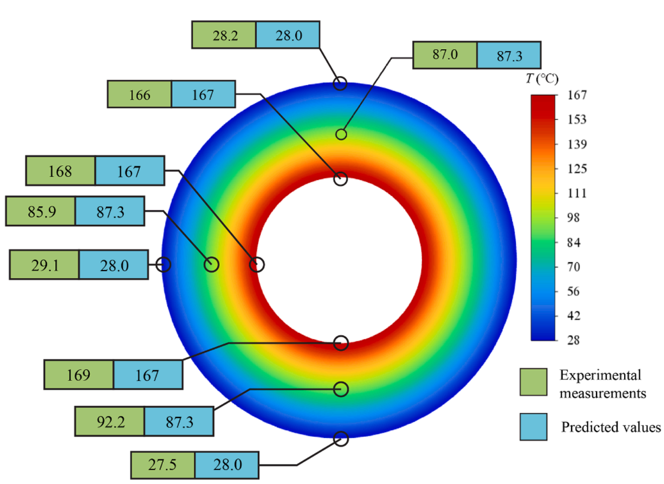

Fig. 3. The predicted steady-state temperature distribution of the insulation, and the interstitial temperature are given (locations 9, 10, 11 in Fig. 1).

3.3. Three simulation models

Three simulation models are built with different characteristics and features to represent different stages of the experiments.

3.3.1. Model 1: 1-D (axisymmetric)

This model does not include gravity. It is used to simulate the dry period, predicting the axisymmetric transient conduction leading to a

Table 4
Submerged-period simulation conditions.

$r = R_i$	Inner boundary temperature T_i (°C)	102
$r = R_o$	Variable pressure (Pa)	$\rho gH - (1-\varepsilon)s_l\rho gy$
	Liquid inlet temperature, T_o (°C)	66.0
	Saturation $s_{l,\ o}$	0.85
Phase change model	Evaporation f (Hz)	0.05
	Condensation f (Hz)	0.05
Heat transfer between phases	Ranz-Marshall model [22]	
Species Transport	Mass diffusivity α (m^2/s)	1.44 × 10^5
Gas Mixture	Thermal Conductivity k (W/m - K)	0.454
	Viscosity μ (kg $/m-s$)	1.72 × 10^{-5}
Relative permeability and capillary pressure	Relative permeability exponent q	3
	Capillary pressure $p_{c,o}$ (kPa)	6 [28]
	Irreducible liquid saturation $s_{l,ir}$	0.05
	Capillary pressure, n	1.6
$t = 0$	Uniform saturation s_l	0.1
	Uniform temperature (°C)	66.0
	Water-vapor mass fraction, x_{H_2O}	0.18

Table 5
Comparison of measured and predicted temperature at various locations at the end of the submerged period (steady state).

Location	Experiment, T (°C)	Prediction, T (°C)	Location	Experiment, T (°C)	Prediction, T (°C)
1	161	–	8	92.0	91.0
2	150	–	9	95.6	93.8
3	66.0	66.0	10	89.7	82.5
4	15.3	–	11	69.0	66.0
5	102	102	12	68.3	66.2
6	101	102	13	65.9	66.0
7	100	98.6	14	64.3	66.0

steady state. The inner and outer surface temperatures are prescribed. This model is valid when the role of gravity in fluid motion is not significant and its implementation results in computing time saving [27].

3.3.2. Model 2: 2-D with gravity and no tank

This model simulates the insulation region using a user-defined pressure inlet. By patching the cell adjacent to the outer boundary, it allows to simulate the hydrophobicity and allows for vapor escape.

3.3.3. Model 3: 2-D with gravity and tank

This simulation model uses a cylindrical mesh for the insulation region and a rectangular mesh for the water tank (liquid region). This does not allow for the control of the outer insulation surface hydrophobicity (liquid saturation).

Table 2 summarizes the three CFD simulation models and attributes.

4. Dry period

In the dry condition, the temperature distribution inside the cylindrical-shell mineral wool insulation follows the logarithmic relation [19]

$$T(r) = T_i + \frac{T_o - T_i}{\ln(R_o/R_i)} \ln(r/R_i), \tag{23}$$

where T_i and R_i are the temperature and radius at the inner surface; and T_o and R_o at the outer surface.

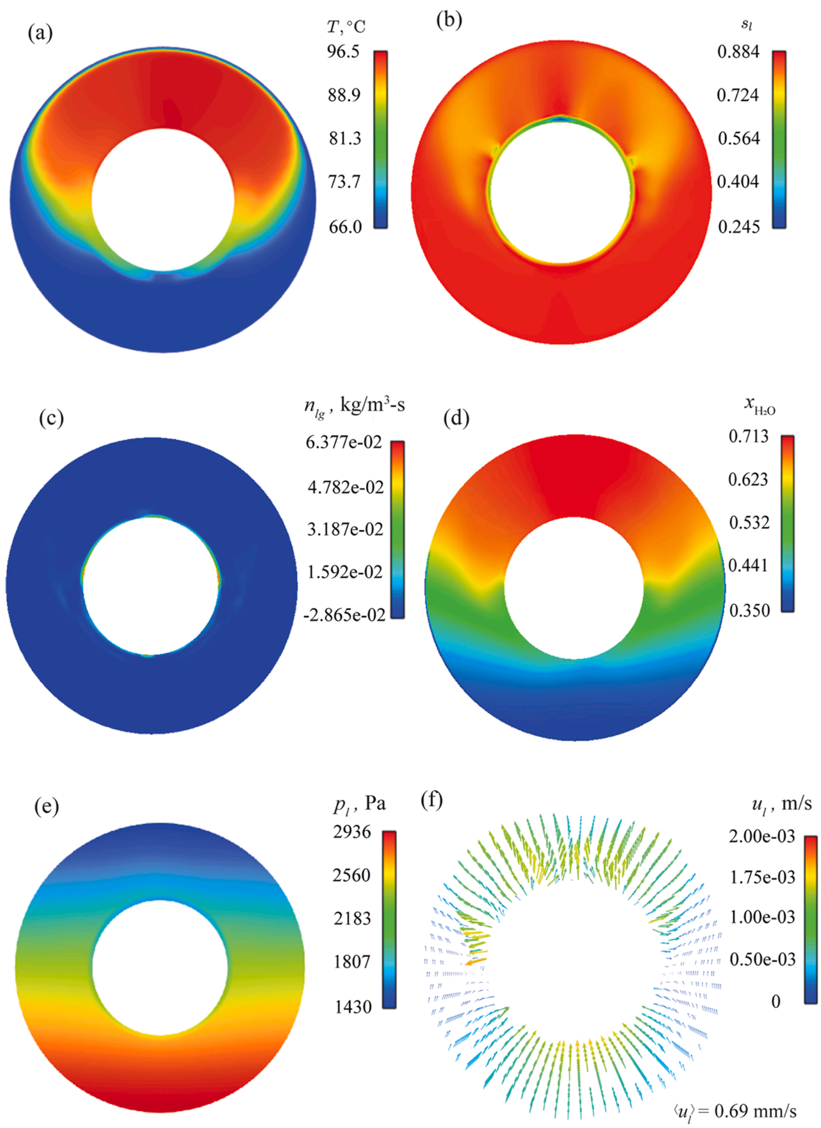

Fig. 4. The predicted steady-state (a) temperature, (b) liquid saturation, (c) evaporation rate, (d) vapor mass fraction, and (e) liquid pressure distributions in the insulation during the submerged period. The interstitial temperature of three different angular locations are listed (locations 9–11, in Fig. 1). The predicted (f) velocity vector and magnitude distributions. In (f), the region adjacent to the pipe surface is excluded since the velocity vector cannot be properly displayed graphically.

The conduction heat flow rate is

$$Q_k = \frac{2\pi k L (T_i - T_o)}{\ln(R_o/R_i)} . \tag{24}$$

Using the data from Table 1, the analytically predicted conduction heat flow rate $Q_k = 49.8$ W, and the predicted interstitial temperature is 89.0°C.

For the prescribed temperature boundary condition of the inner insulation surface, the heat transfer between the pipe and oil is not directly addressed. Instead, the temperature of the pipe outer surface was directly measured, which demonstrates stability throughout the tests. In particular during the dry and submerged periods, the temperature T_7, the thermocouple at 9'o clock on the pipe surface, shows a stable and consistent temperature. Consequently, a constant surface temperature assumption is made for the inner insulation boundary. The simulations do no not include axial variations (limited to 2-D cross section), so an axially average axial surface temperature is used. This was corroborated by the readings of thermocouples $T_{5,6,7,8}$ in Table 3 (with their locations depicted in Fig. 1), demonstrating minimal variations along the axial direction. Hence, the inclusion of the oil side heat transfer was limited to the heat loss by the oil based on inlet and outlet temperatures. The boundary condition of the outer boundary is the so-called pressure outlet with a fixed temperature (25°C). The test results show a daily cyclic variation in the ambient air temperature. This is not included in the simulations which are for lapsed times up to tens of minutes, for practical computational sake.

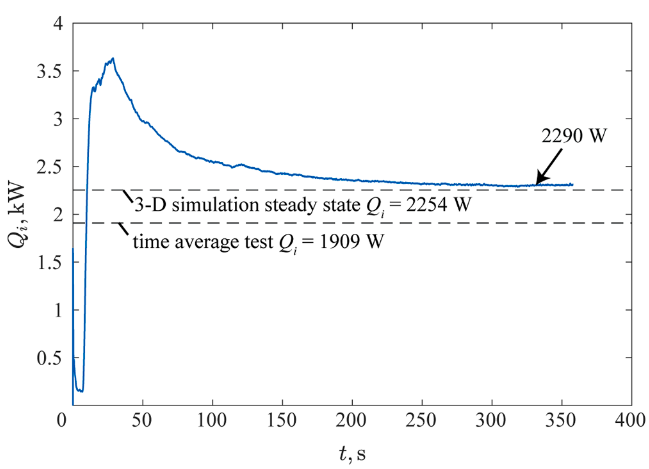

Fig. 5. Variation of measured heat flow rate across the inner boundary of the insulation with respect to time, during the submerged period. The predicted steady-state heat flow rate from the 3-D simulation is also shown, along with the time-averaged measurement value.

The model 1 simulation results in conduction heat flow rate, Q_k= 48.0 W, and the interstitial temperature is 87.3°C. The difference between analytical and simulation results is within 5%. The predicted steady-state temeprature distribution of the insulation is shown in Fig. 3, the comparison of measured and predicted values are both shown.

Table 3 compares the measured and predicted temperature at various locations, at the end of the dry period (steady state). Good agreement is found, for this steady-state conduction within the dry cylindrical shell insulation.

5. Submerged period

The submerged period simulation includes multiphase liquid-vapor flow, capillary pressure, and phase change, which has to be solved numerically. Model 2 from Table 2 allows for controlling the surface liquid saturation to simulate the surface hydrophobicity of the mineral wool. The computation domain ends on the outer-surface of the insulation. Model 3 computation domain contains the submersion tank, and Fluent does not allow for controlling the insulation outer-surface liquid saturation (since it is an internal boundary and is prohibited from prescription).

To simulate the two-phase flow (liquid water and air-water vapor gas mixture), the Fluent Eulerian model, which allows for simulating capillary pressure, is used. The species transport model is activated to simulate the diffusion of condensable (water) and incondensable (air) species. The governing equations are Eqs. (11) and (16).

The thermal boundary condition for the inner boundary is T_i = 102°C. Similar to the dry period constant temperature boundary condition, supported by $T_{5,6,7}$ in Table 5. There is an angular variation between T_7 and T_8 caused by liquid motion. and the outer boundary is the pressure inlet with

$$p_o(y) = \rho g H - (1 - \varepsilon) s_l \rho g y, \tag{25}$$

where y is along the vertical axis, H is the water depth at the center of the insulation. The inlet pressure is determined by the hydrostatic pressure caused by the surface partial saturation (indication of hydrophobicity) of the mineral wool. The liquid comes into the porous matrix with a fixed temperature T_o, defined as the temperature of water in the tank measured at the steady state of the submerged period, which is shown in Table 4.

For the phase change, the Lee model [26] is used with a user-defined evaporation/condensation function and frequency. The governing equations are Eq. (18).

Among the capillary pressure models in Fluent [22], the van-Genuchten model, Eq. (17), is used because of its higher saturation derivative in the high saturation regime. This results in the proper water hold up in the drainage period. The simulation conditions and parameters for the submerged period are listed in Table 4. The uniform liquid

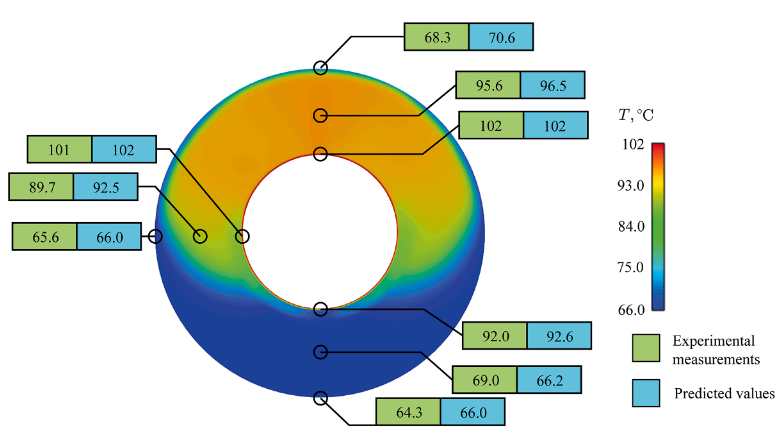

Fig. 6. The predicted steady-state temperature distribution. The measured results are also shown in green rectangles with predicted values in blue rectangles.

saturation starts at 0.1 for convergence purposes. When the simulation starts with zero liquid saturation, the simulation does not converge, due to a very large capillary pressure gradient.

The entry capillary pressure $p_{c,o}$ is empirically selected, guided by the data from [28]. Finding a theoretical guided value, including the fiber contact angle and pore structure and dimension, is currently beyond the scope of this study. To decrease the time to reach steady state, a uniform initial temperature of 66.5°C is used with a corresponding water vapor mass fraction of 0.18 (total pressure of 1 atm) determined from Clausius-Clapeyron relation, Eq. (19). During the submerged period, especially when the system is at steady state, the outer boundary temperature is close to the tank water temperature, which is treated as a constant temperature boundary. This is supported by readings of T_3, T_{12}, T_{13}, and T_{14} in Table 5.

The capillary pressure uses the contact angle for the fiber wettability, and we have used 60° as the average wetting behavior of fiber over the temperature range. Making the fiber contact angle a function of temperature, etc., was not attempted due to lack of data and also due to limitations of the Ansys Fluent.

The soaked insulation mass was measured at the end of the submerged period. The measured mass corresponds to the average liquid saturation, $\langle s_l \rangle$ of about 0.85. With the green (unused), hydrophobic mineral wool insulation, water does wet its surface at room temperature, and our benchtop tests have shown that the liquid saturation can only reach 0.3 at the steady state. However, upon submersion in hot water, the binder and other solvents used for the hydrophobicity dissolve, and the insulation surface becomes more hydrophilic; the liquid saturation can reach 0.8 and even higher depending on how much binder is dissolved. This water non-wetting/wetting can be characterized with the surface liquid saturation. With a green (fresh) sample at room temperature, the surface liquid saturation is low, while under submersion and high temperature, this surface liquid saturation is high. We have used a liquid surface saturation of 0.85 in the submerged period. In the simulations, it takes no more than 2 min to reach the uniform, maximum liquid saturation, $s_{l,o} = 0.85$ (Table 4), and approximately 20 min to reach the thermal steady state. The predicted temperature, liquid saturation, evaporation rate, water vapor mass fraction, liquid pressure, and liquid velocity-vector distributions are shown in Fig. 4 (a) to (f), respectively. Starting from the liquid velocity, shown in the lower Fig. 4 (f), the cold liquid flows upward into the insulation from the bottom. Thus, in Fig. 4(a), the temperature of the lower part of the insulation is close to 66.5°C, which is close to the water inlet temperature T_o. As the liquid flow flows to the bottom of the pipe surface, as expected the bottom surface temperature (T_8 in Table 5) is lower than the surface temperature at other angular positions ($T_{5,6,7}$ in Table 5). Then the liquid flowing into the gap is heated at the inner boundary and evaporates as shown in Fig. 4(c). The vapor generated displaces the liquid and decreases the liquid saturation close to the inner boundary, as shown in Fig. 4(b). Finally, the liquid leaves from the top of the outer boundary with the vapor, Fig. 4(d), thus raising the temperature of the upper region. Fig. 4(e) and (f) show the liquid pressure and velocity vector distributions. Due to the imposed boundary hydrostatic pressure represented by Eq. (25), significant liquid flow occurs within the insulation, with a net liquid flow upward. There are larger velocity vectors and directorial changes adjacent to the inner boundary, which is caused by the intense evaporation there, and the simulations include the momentum phase interaction between the liquid and vapor phases.

Fig. 5 shows the measured variation of the heat flow rate entering the insulation, Q_i, with respect to time. After an initial drop due to the liquid flow into the gap, the heat transfer by convection and evaporation increases, reaching a peak and then falling to a plateau. The plateau is rather large, i.e., 2290 W. The 3-D simulation predicted value is 2254 W, which is close to the 2-D simulation value. The time average measured value is 1909 W, which is smaller than both predicted values.

Table 5 compares the measured and predicted temperature at various locations, at the end of the submerged period (steady state). Rather good agreement (within 10%) is found between them.

Fig. 6 shows predicted steady-state temperature distributions within the wet insulation at the end of the submerged period. The experimental results are also included at selected positions, constructed based on the data at the inner and outer boundary and interstitial locations temperature recording (locations shown in Fig. 1). A good agreement is found between the experiments and prediction. Note that the cooler water entering from the bottom keeps that region at a lower temperature, while the rising/exiting vapor keeps the top region warmer.

To explore the axial distributions within the mineral wool, 3-D simulations are conducted, and the results are presented in Supplementary Materials B: (iv) 3-D simulations, in Figure B.5. The angular–radial liquid saturation non-uniformity found in the upper portion of the 2-D simulations, also appears in the 3-D results with an additional axial non-uniformity [Figure B.5(b)]. This axial non-uniformity is caused by the thermal and phase buoyancy, the latter due to the density difference between liquid and vapor and the non-uniform liquid saturation distribution. This makes the 3-D simulations subject to more numerical instabilities, requiring a smaller time step and mesh size. In general, the 2-D simulation results reveal a more simplified presentation of the spatial distributions, but at substantially lower and achievable computation time.

6. Drainage-drying period

6.1. Drainage subperiod

Drainage subperiod begins when the tank is drained and the liquid held in the insulation begins to drip out of the system. The dripping lasts approximately 20 min. No experimental data is taken, but the video allows for an estimate of the liquid loss rate (decrease in the average saturation $\langle s_l \rangle$) The numerical simulation of the period is also performed

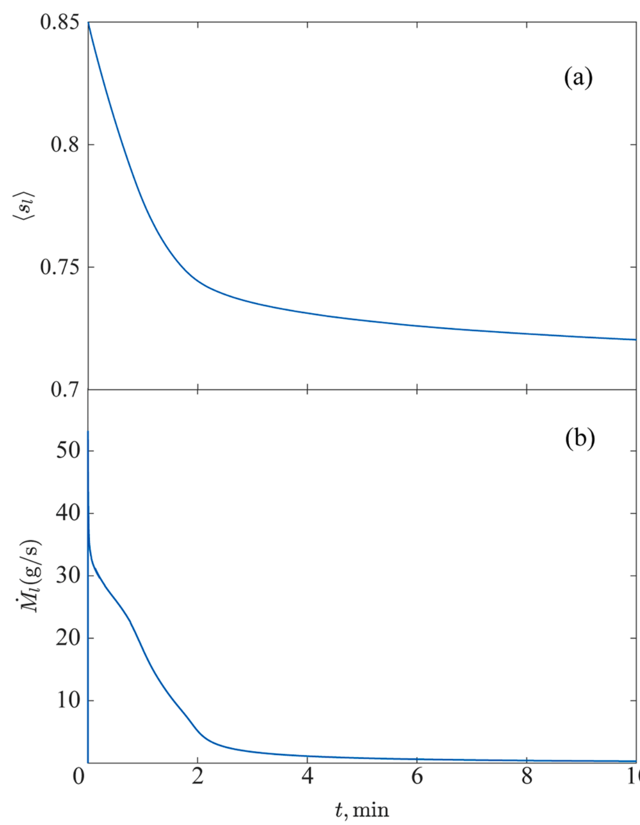

Fig. 7. Time variations of the predicted (a) average liquid saturation, and (b) liquid loss rate during the drainage subperiod.

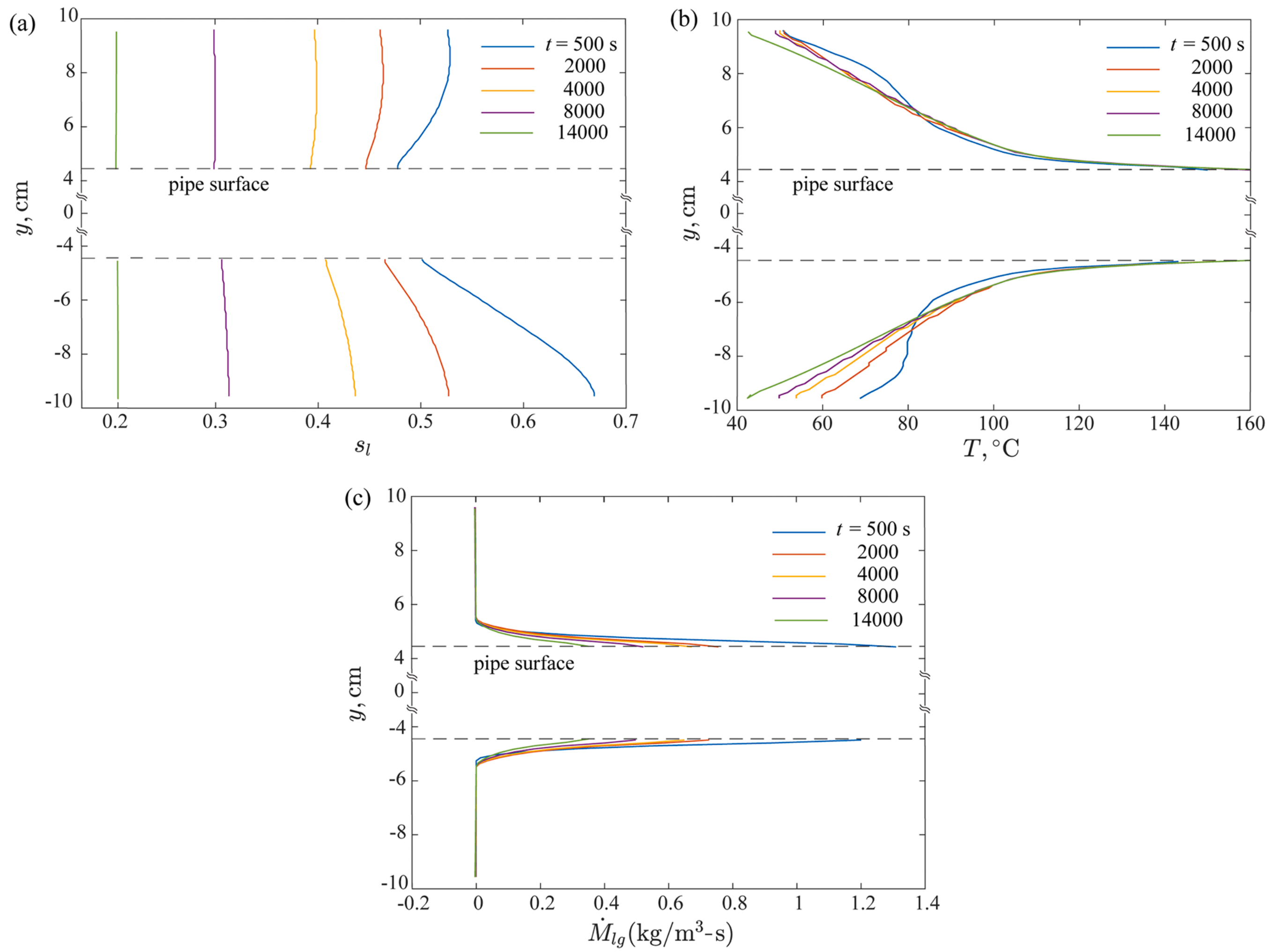

Fig. 8. Predicted spatial (along the vertical axis passing through the pipe center) distributions of (a) liquid saturation, (b) temperature, (c) volumetric evaporation rate, during the drying period, for five lapsed times.

and the results are shown in Fig. 7(a) and (b). As expected, Fig. 7(a) shows a rather high initial rate of drop in the liquid content, followed by an asymptotic drainage stop (no longer dripping). Fig. 7(b) shows this trend in the liquid loss rate. A video of the drainage, right after lowering the water tank, is included in the Supplementary Materials.

6.2. *Drying subperiod*

6.2.1. *Funicular regime: 2-D simulations* ($\langle s_l \rangle > 0.2$)

The funicular regime is the period when the liquid phase is continuous and mobile. The drainage-drying period is dominated by drying, starting with high liquid saturation and ending with the steady dry state. Fig. 8(a) to (c) show the predicted vertical (through the pipe center), y, variations of the liquid saturation, temperature, and volumetric evaporation rate, $\dot{n}_{lg}$, at four elapsed times (referenced to the start of the drainage-drying period). Since the saturation decreases with time and becomes uniform, the capillary pressure dominates over the gravity. The liquid intrusion pressure caused by capillary force can be over 10 kPa [28]. At large elapsed times, the temperature distribution tends toward the logarithm relation of the dry insulation. The evaporation is large adjacent to the heated pipe (inner boundary of insulation) and decreases with time, ending with the dry insulation. A video of the transient liquid saturation distribution during the high saturation period ($1200 < t < 8000$ s) is available in the Supplementary Materials.

6.2.2. *Funicular regime: 1-D simulations* ($0.05 < \langle s_l \rangle < 0.2$)

The reason for choosing $s_l = 0.2$ to switch from 2-D to 1-D simulations is that for saturation larger than 0.2 the gravity effect is signifi-

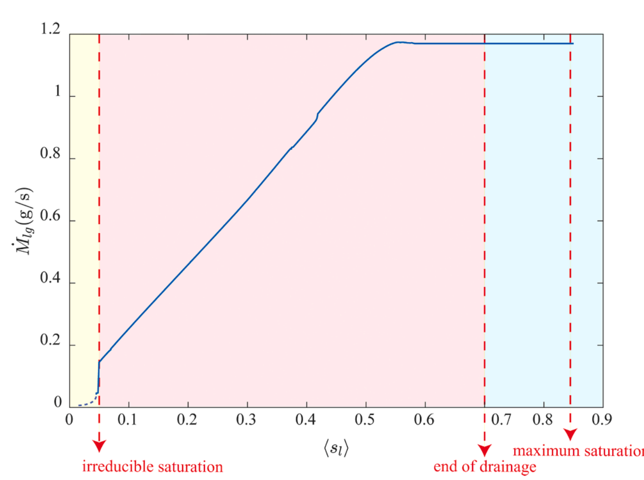

Fig. 9. Predicted variation of the evaporation rate with respect to the average saturation during drainage-drying period. From right to left, constant, linearly decreasing, and falling evaporation rate regimes. The transition average saturations are also marked.

cant resulting in non-uniform (radial and angular liquid) saturation distribution. As for saturation below 0.2, the capillary pressure dominates (over gravity) in the momentum conservation equation; and we have a nearly uniform and axisymmetric distribution of the liquid saturation, temperature, and phase change rate. This is also shown in Fig. 10, where for $t = 3.83$ hr, the liquid saturation, temperature, and evaporation rate distribution are axisymmetric. For the 1-D simulation, a thin vertical strip is used to simplify the simulations and decrease the computing time.

6.2.3. Evaporation-front (Pendular) regime ($\langle s_l \rangle < 0.05$)

Once the average saturation falls below 0.05, as shown in Fig. 10 (a), the region adjacent to the heated surface dries out locally. The irreducible saturation $s_{l,ir}$ is reached, and this immobile liquid evaporates leading to local dryout. Then this dry region extends into the rest of the wet insulation, and this is referred to as the propagating drying-front regime or evaporation-front regime.

Fig. 9 shows the predicted variation of the evaporation rate as a function of the volume-average liquid saturation $\langle s_l \rangle$ during the drainage-drying period. Starting from the maximum saturation $s_{l,o} = 0.85$ (Table 4) on the right, there is the constant evaporation rate regime, where there is significant drainage and liquid motion. The end of the drainage subperiod is marked with $\langle s_l \rangle = 0.7$, and the evaporation rate begins to decrease linearly with the average liquid saturation. According to Eq. (9), as the liquid saturation decreases, the relative permeability decreases and the resistance of liquid flow increases, and this results in a lower evaporation rate. When the average liquid saturation reaches about 0.05, the dry-front appears and the evaporation rate decreases drastically. The various drying regimes and their corresponding average saturations are marked in Fig. 9.

Figs. 10(a) to (c) show snapshots of the liquid saturation, temperature, and evaporation rate distributions, at different marked elapsed times. The wet insulation starts with $\langle s_l \rangle = 0.85$ during the drainage period, and due to the dominance of gravity (over the capillary

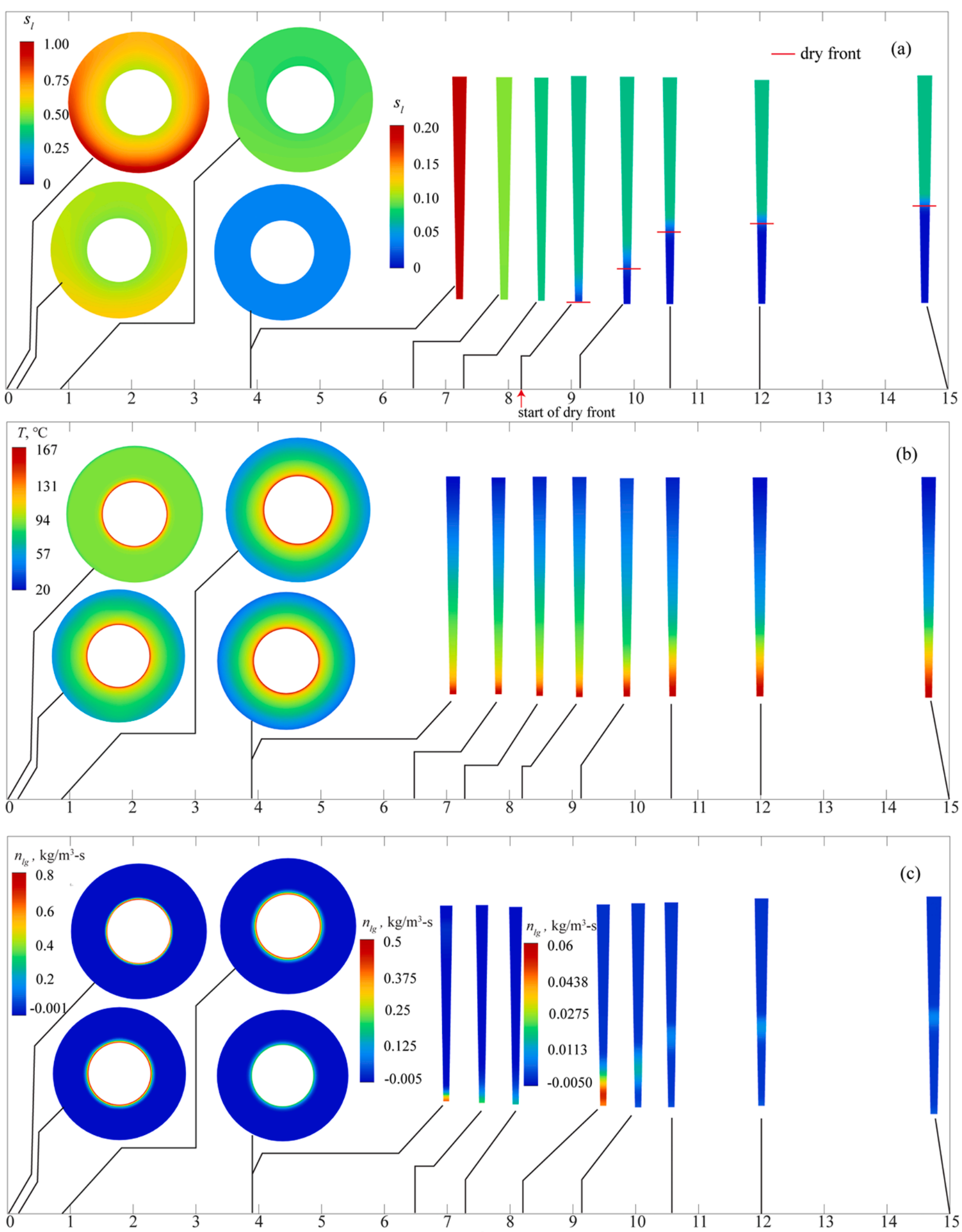

Fig. 10. Snapshots of the predicted (a) liquid saturation, (b) temperature, and (c) evaporation rate distribution in different elapsed times in the drainage-drying period. The early time is simulated using 2-D geometry, while the later time (the thin fan contour) uses 1-D geometry.

pressure), the liquid flows downward during the drainage subperiod. Water liquid flows through the outer boundary, and gradually the drainage stops, as also evident in Fig. 7(b). At the end of the drainage subperiod, the average liquid saturation $\langle s_l \rangle$ drops to 0.7. As $\langle s_l \rangle$ decreases, the capillary pressure increases and gradually dominates, and the liquid saturation distribution becomes uniform. A video of capillary pressure during the early stage of the drying period has been added in the Supplementary Materials. The gauge gas-mixture pressure p_g is 0. The liquid pressure is gas pressure minus the capillary pressure $p_l = p_g - p_c$ [11]. Since all the distributions are rather uniform, Fig. 10(a) to (c), with no angular variations, at t = 3.9 hr, the simulations are switched from model 2 (cylindrical) to model 1 (axisymmetric) as shown in Table 2. As designated in Fig. 10(a), at around t = 8.2 hr, a dry front is formed adjacent to the pipe surface and propagates radially outward.

Fig. 10(b) shows as the outer boundary switches from a prescribed water tank temperature to a heat and mass transfer boundary, the dry-front region appears close to the inner boundary and then propagates. As Shown in Fig. 10(c), the evaporation occurs mostly close to the inner boundary and decreases as $\langle s_l \rangle$ decreases, also evident in Fig. 9. When the dry-front appears and moves outward, the evaporation region moves with it and the evaporation rate drops drastically. Note that the effective thermal conductivity of the insulation decreases to the dry limit of 0.035 W/m − K, and the heat flow rate decreases.

7. Discussions

The measured and predicted results for the three periods are presented as time variations of T (pipe surface and insulation interstitial), Q_i (oil heat loss rate), $\dot{M}_{lg}\Delta h_{lg}$, in Fig. 11(a). For $0 < t < 20$ hr, both the experiment and prediction show an average of Q_i = 60 W. Due to the fluctuation of the ambient temperature, the experimental value also fluctuates. In Fig. 11(a), at t = 20 hr, when the insulation is first submerged, Q_i undergoes a significant increase due to the large temperature difference between the pipe surface and wet insulation. Then the temperature of the pipe increases and with it the wet insulation as well as the water in the tank. The increase in tank temperature and convection in turn decreases the temperature difference between the pipe and the wet insulation, and Q_i decreases with it. When the system is close to the steady state of the submerged period, there is still Q_i of about 2 kW because of convection (liquid motion). The prediction has a shorter time constant because it starts from a higher initial inflow liquid temperature (Table 4). Based on the simulation results, during the submerged period, the heat flow rate through the insulation without a gap is much smaller than the measured value of 2 kW shown in Fig. 11 (without the gap the predicted heat flow rate is only up to 200 W). The liquid is still able to reach the pipe through the capillary action, even without the gap. However, without the gap, the liquid motion (convection) in the wet insulation is about 10 folds smaller than the liquid motion with the gap. Thus, the gap in the simulation setup is essential to have a better match with the measured value. At t = 50 hr, the water in the tank is drained, and liquid leaves from the bottom of the insulation and this stops in about 10 min.

Fig. 11(b) shows the time variation of the measured and predicted interstitial and pipe surface temperature, as well as the measured ambient temperature. The predicted temperature is close to the measured temperature during the dry and submerged periods. In the drying period, the predicted pipe surface temperature T_7 is captured with a rather fast response compared with the experiment. Regarding

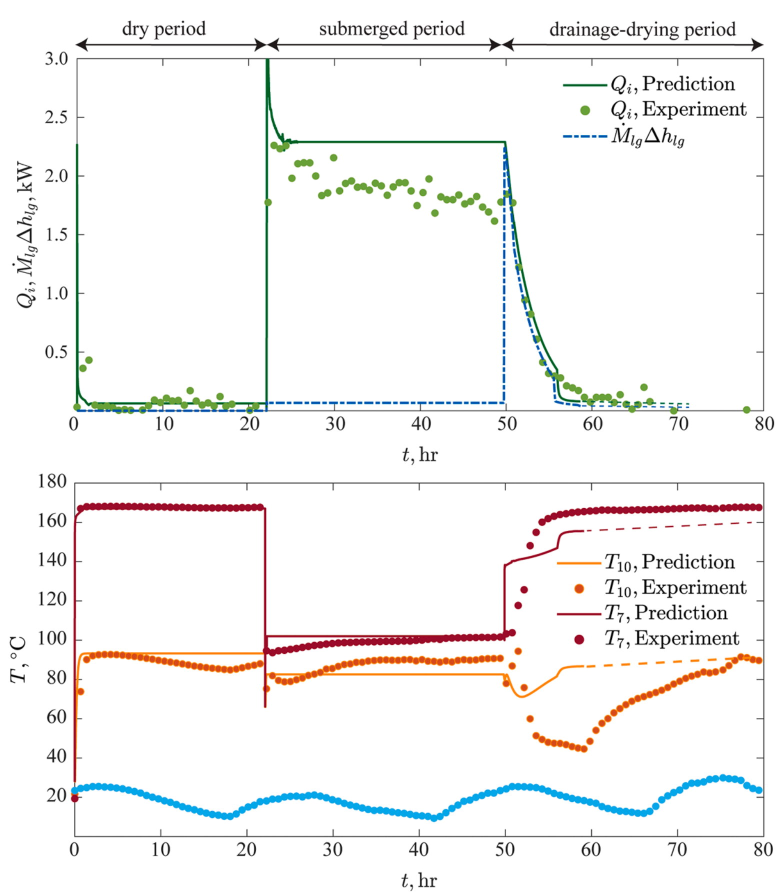

Fig. 11. (a) Experimental and predicted heat flow through the insulation Q_i, and predicted evaporation heat-flow rate, $\dot{M}_{lg}\Delta h_{lg}$ (b) the time variation of the measured ambient (T_4), pipe-surface temperature (T_7), and interstitial temperature (T_{10}), during the three periods. The test data are shown with filled circles, while the predicted results are shown with continuous curves.

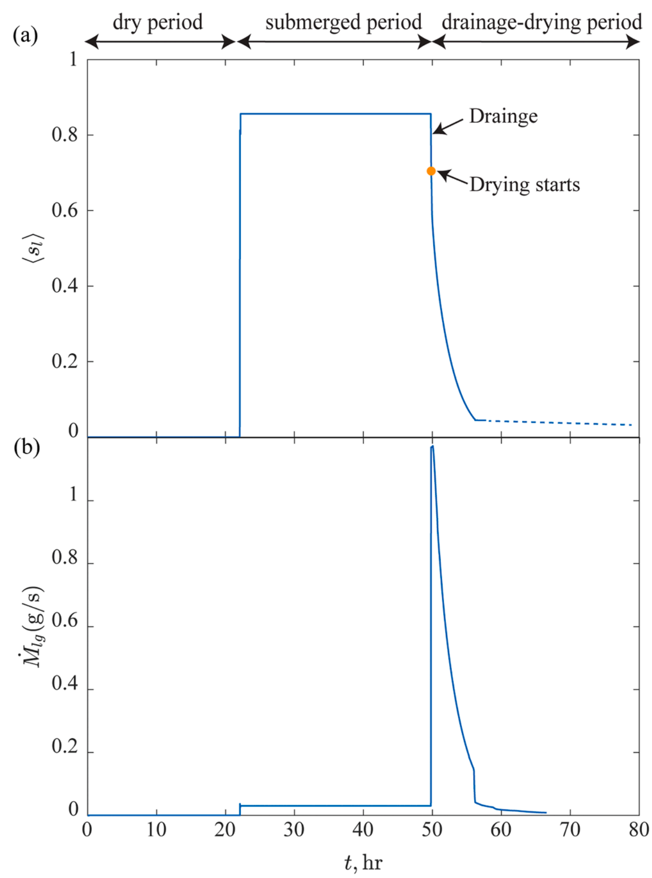

Fig. 12. Predicted time variations of (a) average liquid saturation, and (b) volumetric evaporation rate, through the three periods.

the interstitial temperature T_{10}, there is a large temperature drop in the experiment, while the predicted temperature drops only after the formation of the dry front. The predictions use a constant ambient temperature, so the variation in the ambient temperature could be a major reason. In the simulation, the boundary condition is a convective-heat transfer boundary, with a constant ambient temperature of 25 °C. In the experiments, as shown with the blue dots in Fig. 11(b), the ambient temperature varies between 10 to 25 °C.

Fig. 12(a) shows a steep drop in the liquid saturation, from 0.85 to 0.70 during the drainage subperiod. Right after the short drainage, the liquid convection ceases, however Q_i remains high due to evaporation. For $50 < t < 60$ hr, the liquid saturation decreases due to evaporation

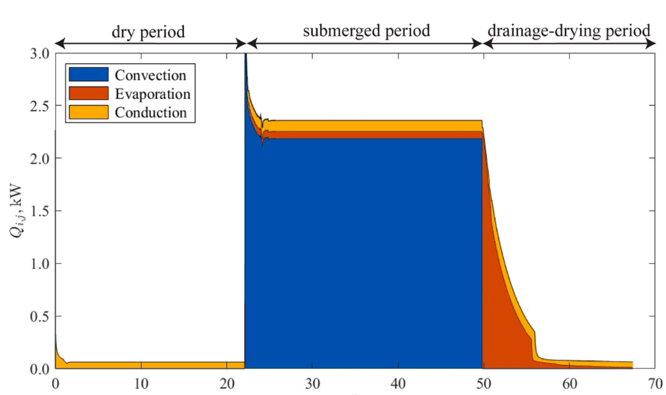

Fig. 13. Division of heat transfer through the wet insulation into conduction (k), convection (u), and evaporation (lg), in each of the three periods, with subscript, $j = k, \boldsymbol{u}, lg$.

and vapor leaves the insulation. Fig. 12(b) shows that the volumetric evaporation rate decreases with time and Q_i. The predicted Q_i is in good agreement with the experimental results during the drying period. In the dry-front regime, Q_i drops significantly, and as the thermal behavior returns to the dry state (Fig. 2), Q_i drops asymptotically to the steady-state dry-period Q_i.

Fig. 13 shows the division of $Q_{i,j}$ into conduction (k), convection ($\boldsymbol{u}$), and evaporation (lg), in each period. In the dry period, there is conduction only, with relatively low effective thermal conductivity. In the submerged period, convection heat transfer (liquid motion inside the wet insulation) dominates with cold liquid entering the insulation from the bottom and being heated inside the gap, then leaving the insulation from the top at a rather high temperature. Heat loss due to evaporation is not large, since condensation occurs in locations within the insulation where water vapor density is larger than the saturation density, also observed in [29]. During the drainage-drying period, convection ceases, and evaporation dominates the heat transfer and decreases as the liquid saturation till complete dryout.

The large heat loss caused by liquid convection is evident during the submerged period. While the increase in conductive heat loss of the wet insulation (due to the increase of thermal conductivity) is known and expected [7,14], the contribution of the convective heat loss, especially in submerged mode is noteworthy. The liquid has substantial mobility at high liquid saturation (relative permeability approaching unity). The experiments and the predictions, when combined, show that submerging causes very large heat loss, here about 2 kW per meter.

8. Conclusions

The undesirable water penetration (imbibition) into fibrous insulation, through the surface or seams exposed to elements, when passing an immobile liquid threshold, can significantly alter the heat flow through the insulation. To investigate this using mineral wool wrapped around a pipe heated to over 100°C, the heat flowing through the dry, water submerged, and drying insulation is measured and also predicted using CFD simulations.

- The liquid motion has a significant impact on the heat transfer rate.
- The heated, soaked insulation hydrophobic agent dissolves thus deteriorating the hydrophobicity and allowing for higher liquid saturation, and therefore intensifying the convection (advection) heat transfer.
- In the submerged period, water reaches the unavoidable small gap between the pipe and the insulation, causing a significant drop in the insulation temperature in that region. The presence of the gap, and the liquid within it, keeps the pipe surface temperature close to the boiling temperature, i.e., a significant temperature drop (about 70°C) from the end of the dry period, and this evaporation increases the heat loss rate.
- In addition to the liquid saturation and capillary pressure, both gravity and hydrostatic pressure affect the liquid motion and heat transfer, with liquid flowing in from the lower and leaving from the upper surface of the insulation.
- The water vapor movement also influences the liquid motion.
- As expected, the highest heat transfer rate occurs during the submerged period, followed by the drainage-drying period where it gradually falls back to the dry period rate. The predicted evaporation rate in the submerged period is not the highest. During the drying period, since the water vapor is able to flow more readily due to low liquid saturation, evaporation (phase change) dominates the heat transfer.
- The last stage of the drying period is marked by the dry-front propagation. This funicular regime (liquid saturation above the irreducible saturation) and the evaporation-front regimes in the drying period are similarly observed in the surface-convection drying [24].

- Also, as expected, the dry period is controlled by conduction, the submerged period by liquid convection, and the drainage-drying period by evaporation.

Good agreement (within 20%) is found between the measurements and the predictions. In the predictions, the van Genuchten capillary pressure model is found to be the most suitable for the high liquid hold up observed in the experiments.

CRediT authorship contribution statement

Fan Lu: Writing – review & editing, Writing – original draft, Visualization, Validation, Methodology, Investigation, Formal analysis, Data curation, Conceptualization. **Massoud Kaviany:** Writing – review & editing, Writing – original draft, Validation, Supervision, Resources, Project administration, Methodology, Investigation, Funding acquisition, Conceptualization. **John Williams:** Writing – original draft, Validation, Supervision, Resources, Project administration, Methodology, Investigation, Funding acquisition, Data curation, Conceptualization. **Thomas Addison-Smith:** Writing – original draft, Resources, Methodology, Data curation.

Declaration of competing interest

The authors declare that they have no known competing financial interests or personal relationships that could have appeared to influence the work reported in this paper.

Data availability

Data will be made available on request.

Acknowledgment

We are thankful to Bryan Veyera for assistance in the tests and for comments on the manuscript draft, and to Eric Gagnon, Grant Nuttall, and Mark Krajewski for their assistance with the test setup and experiments.

Supplementary materials

Supplementary material associated with this article can be found, in the online version, at doi:10.1016/j.ijheatmasstransfer.2024.125644.

References

[1] J. Whetsell, M. Altan, Investigation of hygrothermal effects on the thermal conductivity characteristics of insulation materials, Annu. ASHRAE Trans. 121 (2015).
[2] L.D. Hung Anh, Z. Pásztory, An overview of factors influencing thermal conductivity of building insulation materials, J. Build. Eng. 44 (2021) 102604.
[3] A.M. Papadopoulos, State of the art in thermal insulation materials and aims for future developments, Energy Build. 37 (2005) 77–86.
[4] D. Balaji, S. Sivalingam, et al., Aerogels as alternatives for thermal insulation in buildings – a comparative teeny review, Mater. Today: Proc. 62 (2022) 5371–5377.
[5] Williams, J., Evans, O., "The influence of insulation materials on corrosion under insulation", In: NACE Corrosion conference, Huston, USA: NACE International, 2010.
[6] Q. Cao, T. Pojtanabuntoeng, et al., A review of corrosion under insulation: a critical issue in the oil and gas industry, Metals. (Basel) 12 (2022) 561.
[7] M. Chyu, X. Zeng, L. Ye, Effect of underground water attack on the performance of mineral wool pipe insulation, ASHRAe Trans. 104 (1998) 168.
[8] J. Fan, X. Wen, Modeling heat and moisture transfer through fibrous insulation with phase change and mobile condensates, Int. J. Heat. Mass Transf. 45 (2002) 4045–4055.
[9] C. Hedlin, Heat transfer in a wet porous thermal insulation in a flat roof, J. Therm. Insul. 11 (1988) 165–188.
[10] W. Pei, F. Ming, et al., A thermal conductivity model for insulation materials considering the effect of moisture in cold regions, Cold. Reg. Sci. Technol. 207 (2023) 103770.
[11] M. Kaviany, Principles of Heat Transfer in Porous Media, Springer, New York, 1995. Second Edition.
[12] F. Ahmad, M. Talbi, et al., Non-local equilibrium continuum modeling of partially saturated drying porous media: comparison with pore network simulations, Chem. Eng. Sci. 228 (2020) 115957.
[13] Mokon, "DELF 600 data sheet," [Online]. Available: https://www.mokon.com/products/heat-transfer-oil-systems/heat-transfer-fluids/pdf/delf-600-data-sheet.pdf. [Accessed 9 June 2023].
[14] Kosiński, P., Wójcik, R., Skoratko, D., and Attia, S., "An impact of moisture content on the air permeability of the fibrous insulation materials", International Building Physics Conference, 2069:01225, 2021.
[15] Kosinski, P., Brzyski, P., "Comparison of air permeability and thermal properties of loose mineral wool and hemp fibers", AIP Conference Proceedings, 2305:020007, 2020, https://doi.org/10.1063/5.0034846.
[16] K. Zubarev, V. Gagarin, Determining the coefficient of mineral wool vapor permeability in vertical position, Adv. Intell. Syst. Computi. (Int. Sci. Conf. Energy Manag. Municipal Facilities Sustain. Energy Technol. EMMFT 2019 1259 (2019) 593–600.
[17] Rockwool, "ProRox PS 960″, [Online]. Available: https://rti.rockwool.com/siteassets/applications/wr-tech/rw-ti-prorox-ps-960-wr-tech_en.pdf. [Accessed 29 June 2023].
[18] "Standard practice for inner and outer diameters of thermal insulation for nominal sizes of pipe and tubing (NPS system)", ASME, C585 –22, 2010.
[19] M. Kaviany, Essentials of Heat Transfer, Cambridge University Press, New York, 2011, pp. 426–569.
[20] J.H. Nam, M. Kaviany, Effective diffusivity and water-saturation distribution in single- and two-layer PEMFC diffusion medium, Int. J. Heat. Mass Transf. 46 (2003) 4595–4611.
[21] F. Carrillo, I.C. Bourg, C. Soulaine, Multiphase flow modeling in multiscale porous media: an open-source micro-continuum approach, J. Comput. Phys. 8 (2020) 100073.
[22] ANSYS, Inc., "ANSYS fluent user's guide", Release 17.2, 2021.
[23] Brooks, R.J., Corey, A.T., "Hydraulic properties of porous media", Hydrology Paper No.3, Colorado State University, 1964.
[24] J.A. Rogers, M. Kavainy, Funicular and evaporative-front regimes in convective drying of granular beds, Int. J. Heat. Mass Transf. 35 (1992) 469–480.
[25] M.T. Van Genuchten, A closed form equation for predicting the hydraulic conductivity of unsaturated soils, Soil Sci. Soc. Am. J. 44 (1980) 892–898.
[26] Lee, H.W., "A Pressure Iteration Scheme for Two-Phase Flow Modeling, in: T.N. Veziroglu (Ed.)", Multiphase Transport Fundamentals, Reactor Safety, Applications, vol.1, Hemisphere Publishing, Washington, DC, 1980.
[27] K. Vafai, H., C. Tien, A numerical investigation of phase change effects in porous materials, Int. J. Heat. Mass Transf. 32 (1989) 1261–1277.
[28] Moghadam, A., "Capillary forces in partially Saturated thin fibrous media", Ph.D. thesis, Virginia Commonwealth University, 2019.
[29] K. Vafai, S. Whitaker, Simultaneous heat and mass transfer accompanied by phase change in porous insulation, J. Heat. Transf. 108 (1) (1986) 132–140.